nanomaterials

MDPI

Article

Improving the Photocatalytic Activity of Mesoporous Titania Films through the Formation of WS_2/TiO_2 Nano-Heterostructures

Junkai Ren [1], Luigi Stagi [1], Luca Malfatti [1], Valentina Paolucci [2], Carlo Cantalini [2], Sebastiano Garroni [3], Marzia Mureddu [3] and Plinio Innocenzi [1,*]

[1] Laboratory of Materials Science and Nanotechnology (LMNT), Department of Biomedical Sciences, CR-INSTM, University of Sassari, 07100 Sassari, Italy; j.ren@studenti.uniss.it (J.R.); lstagi@uniss.it (L.S.); lucamalfatti@uniss.it (L.M.)

[2] Department of Industrial and Information Engineering and Economy, University of L'Aquila, 67100 L'Aquila, Italy; valentina.paolucci2@univaq.it (V.P.); carlo.cantalini@univaq.it (C.C.)

[3] Department of Chemistry and Geology, University of Sassari, 07100 Sassari, Italy; sgarroni@uniss.it (S.G.); m.mureddu6@studenti.uniss.it (M.M.)

* Correspondence: plinio@uniss.it

Abstract: Heterostructures formed by anatase nanotitania and bidimensional semiconducting materials are expected to become the next-generation photocatalytic materials with an extended operating range and higher performances. The capability of fabricating optically transparent photocatalytic thin films is also a highly demanded technological issue, and increasing the performances of such devices would significantly impact several applications, from self-cleaning surfaces to photovoltaic systems. To improve the performances of such devices, WS_2/TiO_2 heterostructures obtained by incorporating two-dimensional transition metal dichalcogenides layers into titania mesoporous ordered thin films have been fabricated. The self-assembly process has been carefully controlled to avoid disruption of the order during film fabrication. WS_2 nanosheets of different sizes have been exfoliated by sonication and incorporated in the mesoporous films via one-pot processing. The WS_2 nanosheets result as well-dispersed within the titania anatase mesoporous film that retains a mesoporous ordered structure. An enhanced photocatalytic response due to an interparticle electron transfer effect has been observed. The structural characterization of the heterostructure has revealed a tight interplay between the matrix and nanosheets rather than a simple additive co-catalyst effect.

Keywords: tungsten disulfide; titania; heterostructure; photocatalysis; mesoporous films

Citation: Ren, J.; Stagi, L.; Malfatti, L.; Paolucci, V.; Cantalini, C.; Garroni, S.; Mureddu, M.; Innocenzi, P. Improving the Photocatalytic Activity of Mesoporous Titania Films through the Formation of WS_2/TiO_2 Nano-Heterostructures. *Nanomaterials* **2022**, *12*, 1074. https://doi.org/10.3390/nano12071074

Academic Editors: Filippo Giannazzo and Ivan Shtepliuk

Received: 1 March 2022
Accepted: 23 March 2022
Published: 25 March 2022

1. Introduction

Since the discovery of graphene, the attention of researchers has focused on obtaining other two-dimensional (2D) materials by exfoliation of the parent layered bulk materials or via bottom-up routes [1,2]. Stacks of weakly bonded and atomic thick sheets form the layered materials, and different methods have been developed to exfoliate them into single- or few-layer components. Transition metal dichalcogenides (TMDCs), such as molybdenum disulfide (MoS_2) and tungsten disulfide (WS_2), are among the most studied layered materials whose functional properties enable applications in electronics and photonics [3]. Among TMDCs, WS_2 has attracted particular attention because of its outstanding electronic properties, making it an ideal material for the rational design of photocatalysts and photoelectrodes [4,5]. In fact, the WS_2 bandgap undergoes an indirect (~1.4 eV) to direct (~2.1 eV) transition when the material size is reduced from bulk to monolayer, as an effect of the quantum confinement. WS_2 nanosheets have been combined with other semiconductors, such as g-C_3N_4 [6,7], CdS [8,9], and TiO_2 [10–12], to fabricate heterostructures with enhanced photocatalytic activity for pollutant degradation or water splitting. Although pure TiO_2 is still considered a standard for photocatalysis, the fast hole-charge

recombination rate represents an intrinsic limit [13]. For this reason, the development of titania heterostructures with chalcogenide materials is the subject of intensive investigation in the quest for an efficient method to produce energy from sunlight.

Up to now, nanocrystalline anatase titania (TiO_2) in the form of micro- or nano-particles has represented the first choice for photocatalytic application. The low production cost, the exceptional stability under irradiation, and the ease of synthesis make the nanotitania an excellent photocatalytic material. A few articles have reported the formation of heterostructures based on nanocrystalline titania particles (both dense and mesoporous) sensitized with WS_2 [12,14]. In all cases, the formation of WS_2 occurred in situ on the TiO_2 particle surface via photochemical reduction of $(NH_4)_2WS_4$. The formation of heterostructures, obtained by coupling two semiconductors with different energy levels, besides enhancing the photocatalytic performances under UV-light irradiation [15], could also extend the range of activity to the visible light.

More recently, however, the use of TiO_2 powders and nanoparticles has been severely limited due to the classification as category 2 "suspected carcinogen by inhalation", made by the Committee for Risk Assessment of the European Chemical Agency [16]. Therefore, the synthesis of TiO_2 mesoporous films appears as an attractive alternative. The material in the form of a thin film does not pose inhalation health risks and provides an efficient platform for photocatalysis due to the high surface area. However, the fabrication of optically active heterostructures by integrating 2D layers into mesoporous ordered titania films is still a challenging target to achieve. To the best of our knowledge, there is only one published report about the synthesis of a porous titania coating supporting WS_2 [17]. These heterostructures, however, were prepared by forming a thin layer of 2D nanosheets directly on the porous surface. This synthesis method creates a sharp separation between the titania porous film and the TMDC phase.

In our previous works, we have successfully introduced graphene and boron nitride sheets into titania mesoporous films via evaporation-induced self-assembly [18,19]. This process allows direct incorporation of mechanically exfoliated 2D materials in the precursor sol. The method requires integrating the self-assembly process with the 2D materials without disrupting the self-organization during the film processing. The final nanocrystalline mesoporous matrix is obtained by thermal annealing. After the processing, the 2D materials are homogeneously dispersed within the matrix while preserving the high surface area provided by the mesoporous structure. The fabrication of a robust TiO_2-based heterostructure in the shape of thin mesoporous ordered films is expected to improve the functional properties thanks to the higher surface area and better diffusivity in the pore structure.

TiO_2-WS_2 heterostructures have been fabricated and tested for photocatalysis in the present work. Integration of photoactive heterostructures into functional devices should have a significant impact on improving the photocatalysis performance.

2. Results and Discussion

A critical step in the synthesis of TiO_2-2D WS_2 heterostructures is the production of WS_2 sheets of controlled properties, employing a feasible and reproducible fabrication method. The exfoliation of 2D WS_2 has been achieved by sonication of crystalline WS_2 powders (WS_2-P) in 1-methyl-2-pyrrolidinone (NMP) using a sonicator tip (Scheme 1a). Centrifugation at different rotational speeds has allowed precipitating the unexfoliated aggregates (WS_2-U), and further separating the exfoliated WS_2 into large and small nanosheets (WS_2-L and WS_2-S), respectively. With the reduction of size and dimension, the color of WS_2 dispersions gradually changes from dark grey to brown and yellow. The TiO_2 mesoporous films have been prepared via a template-assisted self-assembly route. The WS_2-TiO_2 heterostructures form by incorporating the WS_2 nanosheets into TiO_2 films in the precursor sol and deposition of thin films by dip-coating (Scheme 1b). During the solvent evaporation, the templating micelles self-assemble into an ordered array while the WS_2 sheets disperse within the matrix without disrupting the self-assembly.

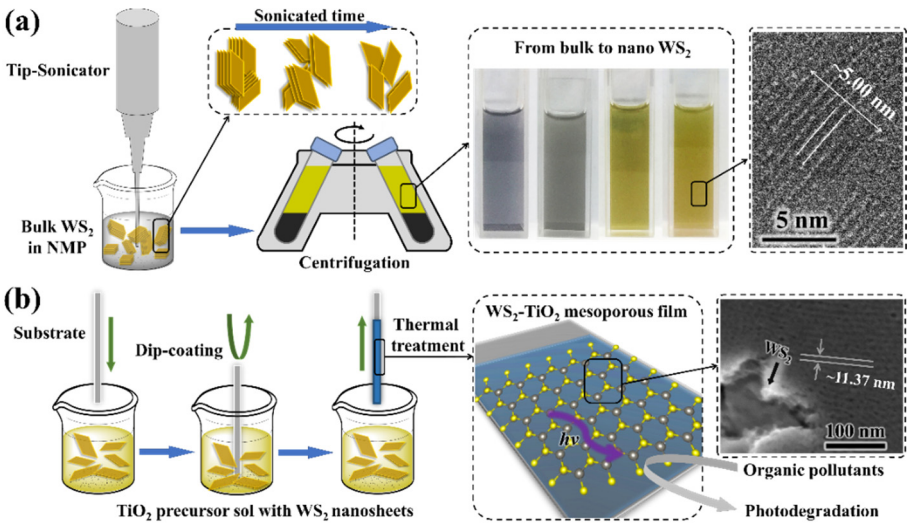

Scheme 1. Schematic of (**a**) the exfoliation of 2D WS_2 nanosheets via tip-sonication, and (**b**) the formation of WS_2-TiO_2 mesoporous film heterostructures via dip-coating.

2.1. Exfoliation of WS_2 Nanosheets

A set of complementary analyses has been used to characterize the size and structure of the WS_2 samples after sonication and centrifugation.

The transmission electron microscopy (TEM) images in Figure 1 confirm that higher centrifugation rates allow for the collection of thinner and smaller nanosheets in the supernatants. The lateral size of unexfoliated WS_2 (WS_2-U) is over 1 µm, and the thickness is in the range of tens of nanometers, suggesting that WS_2-U still shows the bulk crystal characteristics. On the contrary, the exfoliated WS_2 nanosheets have a lateral size in the range of 100–400 nm. The folding edges of WS_2 platelets reported in Figure 1c,f,i enable direct observation of the layered structure through the interplanar distance of the (002) planes. The interlayer d-spacing is ~0.624 nm, which is in good agreement with the value reported for the 2H-WS_2 structure [20]. Interestingly, the thicknesses of WS_2-L (~10 nm) and WS_2-S (~5 nm) are much thinner than WS_2-U, corresponding to ~16 and ~8 monoatomic layers, respectively.

Figure 2a shows the X-ray diffraction (XRD) patterns of the different WS_2 layers' structures. An intense diffraction peak at 14.25° from the characteristic (002) reflection characterizes the 2H-WS_2 phase, and three weaker diffraction peaks at 28.85°, 43.90°, and 59.80° corresponding to the (004), (006), and (008) planes were also detected [21]. According to Bragg's equation, the d-spacing of (002) is ~0.621 nm, in good accordance with the TEM results. The full width at half-maximum (FWHM) of all XRD peaks shows a widening trend when the dimension of WS_2 reduces from the bulk to nanoscale, in agreement with the Scherrer law.

Raman analysis in Figure 2b supports the XRD and TEM results. The bands peaking at ~422.0 and 352.5 cm^{-1} are assigned to the first-order A_{1g} and E_{2g} Raman modes, which originate from the out-of-plane and in-plane vibrations, respectively [22]. A detailed analysis of the Raman bands (Supplementary Figure S1) confirms the size reduction of WS_2 as a function of the sonication treatment. For example, by comparing WS_2-P with WS_2-S, it can be found that the frequency difference of A_{1g} and E_{2g} changed from 69.5 to 68.5 cm^{-1}, the FWHM of the A_{1g} mode widened from 4.32 to 6.18 cm^{-1}, and the relative intensity of A_{1g}/E_{2g} decreased from 1.92 to 1.23.

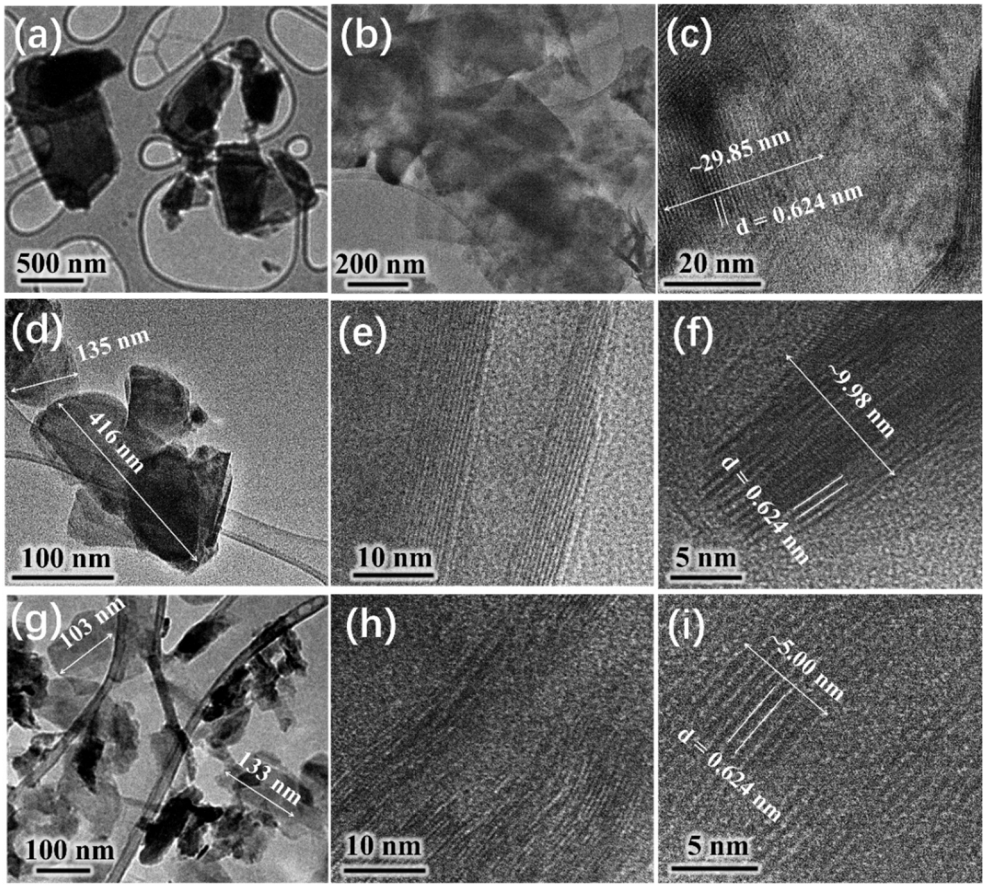

Figure 1. TEM images of the WS_2 products after sonication. (**a**–**c**) WS_2-U, (**d**–**f**) WS_2-L, and (**g**–**i**) WS_2-S.

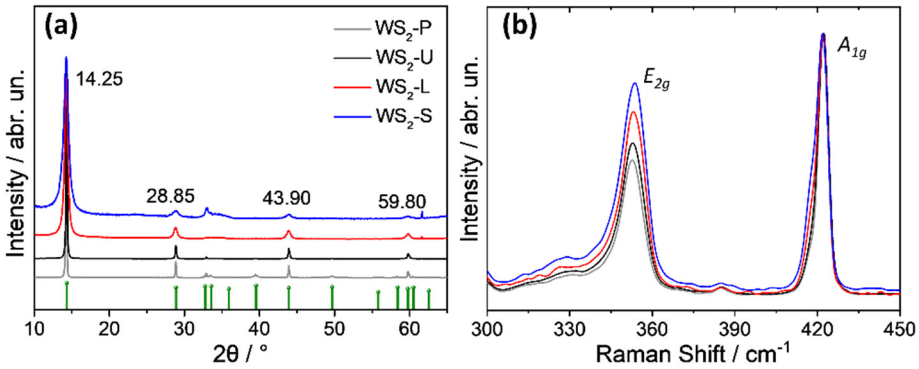

Figure 2. (**a**) XRD patterns and (**b**) Raman spectra of WS_2-P (grey line), WS_2-U (black line), WS_2-L (red line), and WS_2-S (blue line). The green marks at the bottom of (**a**) are the diffraction peaks of 2H-WS_2 (PDF Card ICDD No. 00-008-0237).

Figure 3a shows the UV-Vis absorption spectra of WS_2 dispersions in EtOH. No obvious absorption bands were detected from the bulk WS_2 samples (WS_2-P and WS_2-U) because their indirect bandgap can reach ~1.4 eV [23], which is in the near-infrared region (see Supplementary Figure S2). When the WS_2 size is reduced to the nanoscale, four bands can be distinctly observed (labeled as A, B, C, and D). In the case of WS_2-L, the A and B excitons at 635 and 530 nm originate from the direct gap transitions at the K point in the Brillouin zone, while the C and D bands at 464 and 418 nm are due to the direct transitions from the deep valence to the conduction band [24,25]. In WS_2-S, these absorption bands

show a hypsochromic shift to 629, 523, 456, and 415 nm, respectively, attributed to the quantum confinement in nanosheets [26].

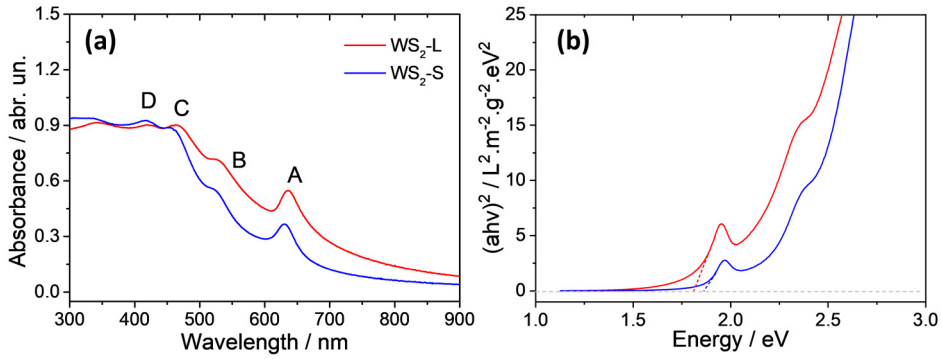

Figure 3. (**a**) UV-Vis absorption spectra and (**b**) Tauc plots of WS_2 nanosheets (WS_2-L red line, WS_2-S blue line).

The band A at 635 nm corresponds to the lowest optical bandgap, which can be evaluated using the Tauc equation (see Figure 3b) [27]:

$$(\alpha h\nu)^n = A(h\nu - E_g) \quad (1)$$

where hν is the photon energy, α is the energy absorption coefficient (calculated from UV-Vis absorption spectra), A is the absorption edge width parameter, E_g is the bandgap, and the exponent n depends on the type of optical transition in the gap region (*n* equals 2 for a direct transition). WS_2-L and WS_2-S have a calculated bandgap of 1.82 and 1.88 eV, respectively. Both these values are higher than the corresponding bulk value of ~1.4 eV and close to the bandgap of ~2.1 eV reported in the literature for a single layer [22]. These results suggest that a reduction of the number of layers can lead to a crossover transition from an indirect bandgap in the bulk to a direct bandgap in the monolayer.

2.2. Construction of WS_2-TiO_2 Heterostructures

The structural and optical properties of mesoporous thin films have been extensively investigated to understand how the insertion of WS_2 nanosheets can affect the heterostructure formation. Bulk WS_2 and their nanosheets (both large and small) have been incorporated into the titania mesoporous matrices to form namely TiO_2-WS2 (U), TiO_2-WS_2 (L), and TiO_2-WS_2 (S) heterostructures, while the undoped TiO_2 was used as a reference film for comparison.

Figure 4a,b shows the field emission scanning electron microscope (FE-SEM) images of the mesostructured titania films after annealing. The image at high magnification indicates that thermal removal of the template leaves a well-organized mesoporous structure. The surface plot analysis provided a wall-to-wall average distance of 11.4 nm for both pure mesostructured TiO_2 and its heterojunction. The TEM images in Figure 4c,d allow more precise observation of the ordered pore arrangement. The morphologies are compatible with a body-centered cubic structure with an Im-3m symmetry [19,28]. According to the Fast Fourier Transform (FFT) patterns, the cell parameter is ~11.8 nm (11.74 nm for undoped TiO_2, 11.93 nm for its heterostructure). The ordered mesoporosity within the nanocomposite films indicates that the presence of WS_2 sheets does not disrupt the self-assembly process.

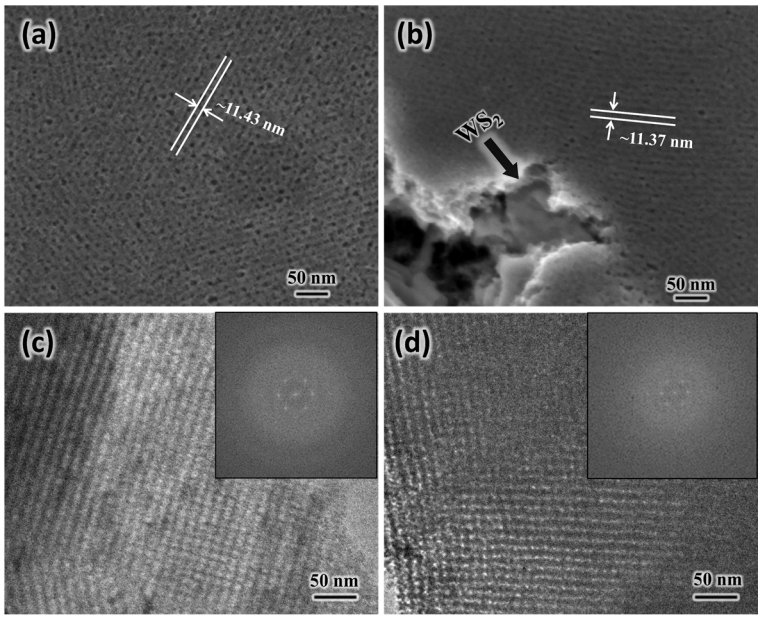

Figure 4. (**a**,**b**) SEM and (**c**,**d**) TEM images of (**a**,**c**) undoped mesostructured TiO_2 and (**b**,**d**) WS_2-doped mesostructured TiO_2 films. The insets in (**c**,**d**) show the corresponding FFT patterns.

XRD patterns and Raman spectra have been collected to determine the crystal structure of TiO_2-WS_2 films deposited on silicon wafer substrates. The two sharp diffraction peaks at 14.25° and 54.36° (Figure 5a) are assigned to the characteristic (002) reflection in the 2H-WS_2 phase (marked by a rhombus ◆) and the (311) plane of the Si wafer surface (marked by an asterisk *). The signals at 25.41° and 55.24° are attributed to (101) and (211) reflections of the anatase phase, obtained from amorphous titania after the annealing process [10,29]. By applying the Scherrer equation to the (101) reflection, we have estimated the anatase crystallite size as 1.78, 1.85, 2.20, and 2.31 nm for TiO_2, TiO_2-WS_2 (U), TiO_2-WS_2 (L), and TiO_2-WS_2 (S), respectively. Despite only minor differences among XRD patterns, the data suggest that the 2D structures promote anatase crystallization via heterogeneous nucleation. Interestingly, this effect is emphasized with the decrease of the WS_2 size, because of the higher specific surface area.

Figure 5b allows comparing the Raman spectra of the different TiO_2-WS_2 heterostructures. The Raman band at 146.5 cm^{-1} and the weak signal at 640.0 cm^{-1} are assigned to the E_g vibration mode of O-Ti-O in the anatase phase [30]. These bands show the same intensity and position in all four spectra. On the contrary, the two sharp bands at ~422.0 and 352.5 cm^{-1}, attributed to the first-order A_{1g} and E_{2g} modes of WS_2, are only present in WS_2-TiO_2 films, suggesting the successful incorporation of WS_2 platelets into the titania layers. Interestingly, no signals were detected from the O-W-O stretching in the range of 750–900 cm^{-1} [31], indicating that the N_2 flow can effectively avoid the oxidation of WS_2 samples during the thermal annealing of the titania films.

Spectroscopic ellipsometry has also been used to estimate the thickness and refractive index of the samples. The films had a similar thickness in the range of 130–140 nm with a general experimental error of ~10 nm (Supplementary Figure S3a), confirming that the incorporation of WS_2 platelets does not cause shrinkage or expansion of TiO_2 thin films. The refractive index of the samples in the 380–900 nm range constantly increased by decreasing the WS_2 nanosheet size (Supplementary Figure S3b), similarly to what was observed for the crystal size of TiO_2 anatase.

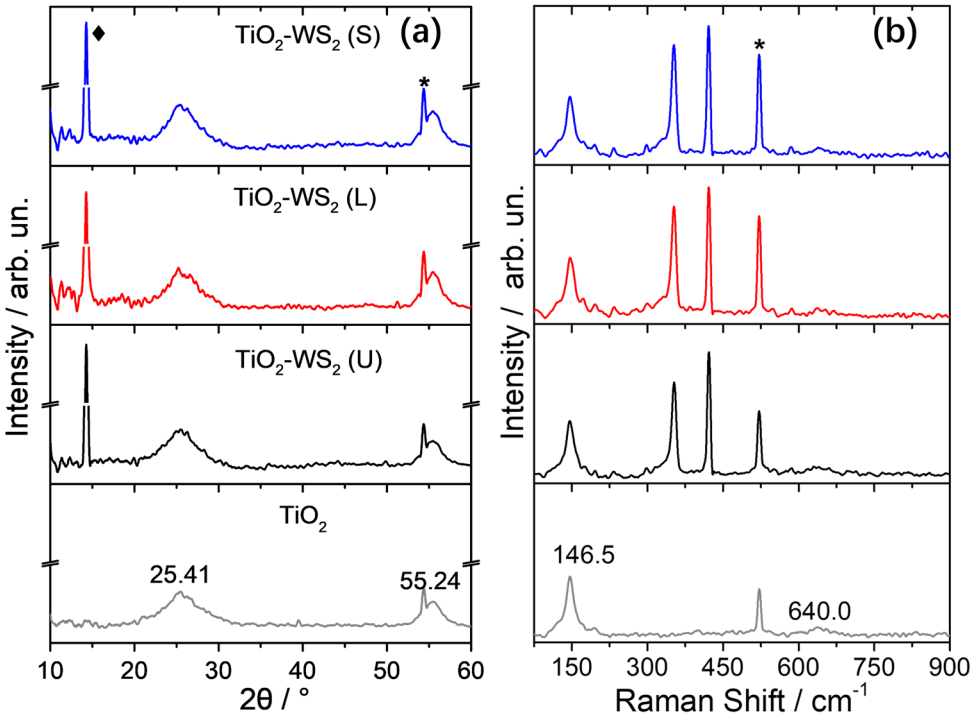

Figure 5. (**a**) XRD patterns and (**b**) Raman spectra of WS_2-TiO_2 films: undoped TiO_2 (grey line), TiO_2-WS_2-U (black line), TiO_2-WS_2-L (red line), and TiO_2-WS_2-S (blue line). The signal at 521.5 cm^{-1}, marked with an asterisk, is caused by the monocrystalline Si wafer.

Figure 6a shows the UV-Vis absorption spectra of the mesoporous films deposited on silica glass substrates. There were no evident differences among these samples, however a closer look at the ultraviolet range revealed that TiO_2-WS_2 (L) and (S) films have a slightly higher absorption (around 0.025 in intensity) than TiO_2 and TiO_2-WS_2 (U). The higher absorption is caused by the incorporation of WS_2 nanosheets (see Figure 3a) which, actually, does not allow observing the A–D bands of layered WS_2 from the UV-Vis spectra of TiO_2-WS_2 films, because of a limited doping amount. The optical transmittance of the four samples (Supplementary Figure S4) allowed for plotting the Tauc curves in Figure 6b, which shows the effect of 2D WS_2 on the bandgap of the films. The bandgap value shifted from 3.31 eV (undoped TiO_2) to 3.30, 3.27, and 3.25 eV, respectively, for the three WS_2-TiO_2 films. In accordance with the previous results, smaller-sized WS_2 sheets contributed to a larger bathochromic shift of the optical gap.

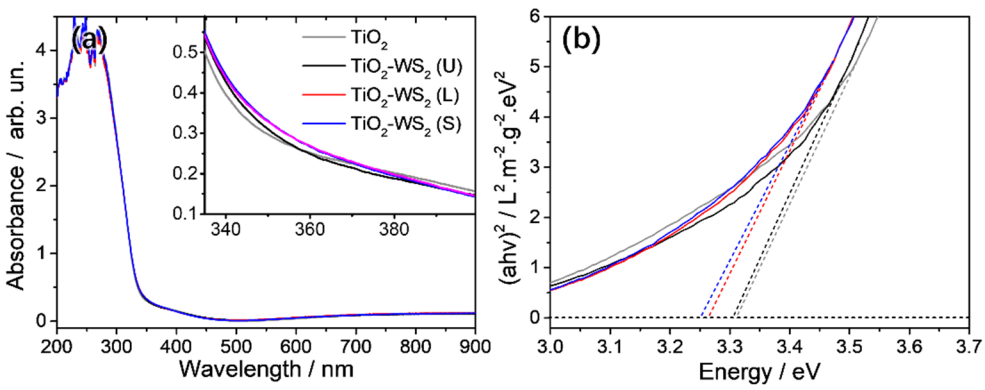

Figure 6. (**a**) UV-Vis absorption spectra and (**b**) Tauc plots of WS_2-TiO_2 films: undoped TiO_2 (grey line), TiO_2-WS_2-U (black line), TiO_2-WS_2-L (red line), and TiO_2-WS_2-S (blue line). The inset in (**a**) shows an enlarged region in the 330–400 nm region.

2.3. Evaluation of Photocatalytic Activity in WS_2-TiO_2 Heterostructures

Stearic acid has been used to measure the photocatalytic response of the heterostructures (Figures S5 and S6) by monitoring the absorption intensity of the -CH_3 and -CH_2 vibrational modes in the 2945–2845 cm^{-1} range using FTIR spectroscopy (see Supplementary Figure S7). The degradation rate of stearic acid (stearic acid/%) has been determined by the following equation:

$$\text{stearic acid}/\% = I_t/I_0 * 100\% \quad (2)$$

where I_t stands for the absorption maximum intensity as a function of irradiation time and I_0 is the initial value of the absorption maximum intensity before exposure (at t = 0). Figure 7a shows the photoinduced degradation curves of stearic acid cast on the different mesoporous films. After around 2 h of UV exposition, ~80% of the stearic acid can be degraded on the four samples. The photodegradation data follow the pseudo-first-order kinetics according to Figure 7b. Therefore, the degradation curves have been fitted by an exponential decay law:

$$I(t) = I_0 * e^{-kt} \quad (3)$$

where the parameter k is the degradation rate. The k value for undoped TiO_2 film was calculated to be ~0.0105 min^{-1}, and the k for the TiO_2-WS_2 (U) film was similar, ~0.0107 min^{-1}, which suggests that the bulk WS_2 does not change the photoactivity of titania. Interestingly, the k values of TiO_2-WS_2 (L) and (S) films (~0.0118 and 0.0121 min^{-1}) showed ≈20% enhancement with respect to bare TiO_2 or TiO_2-WS_2 (U).

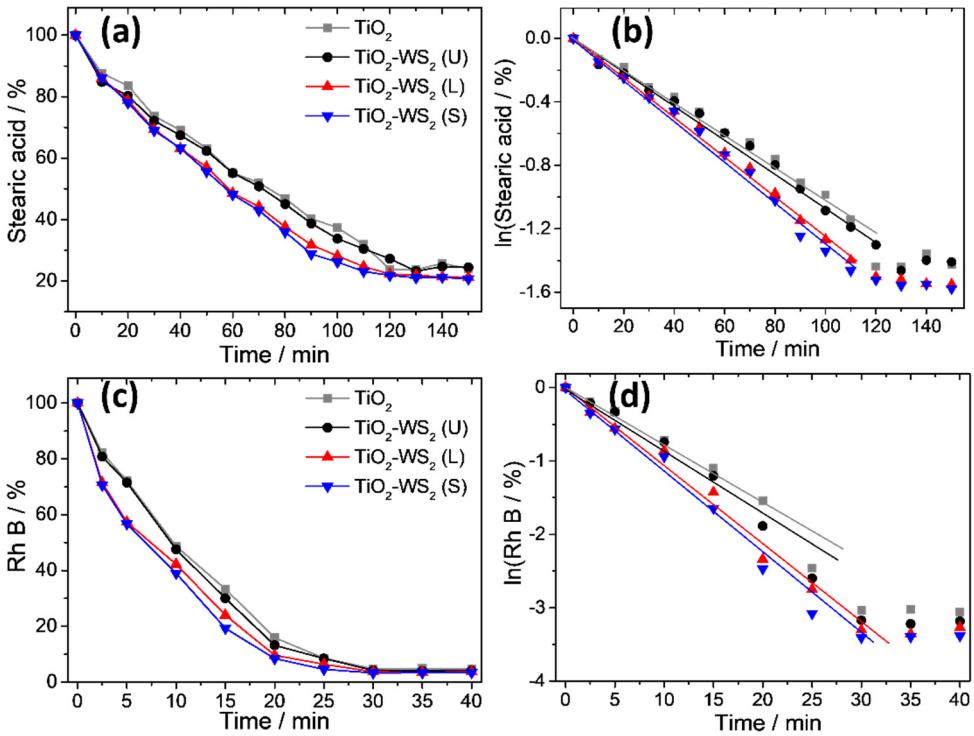

Figure 7. Photoinduced degradation of (**a**) stearic acid and (**c**) RhB on the WS_2-TiO_2 films, and the pseudo-first-order fit of (**b**) stearic acid and (**d**) RhB decay at increasing times of UV irradiation: undoped TiO_2 (grey line), TiO_2-WS_2-U (black line), TiO_2-WS_2-L (red line), and TiO_2-WS_2-S (blue line).

The photocatalytic activity of the heterostructures has also been evaluated using Rhodamine B (RhB) as a probe dye by calculating the absorption intensity in the 450–600 nm region (see Supplementary Figure S8). Figure 7c shows that ~95% of the RhB can be degraded on the four films after the UV exposition of only 30 min. According to Figure 7d, the k values of TiO_2-WS_2 (L) and (S) films (~0.1063 and 0.1102 min^{-1}) exhibited a 35%

improvement compared to bare TiO_2 or TiO_2-WS_2 (U) films (~0.0808 and 0.0843 min^{-1}). It shows a trend similar to stearic acid even if the photodegradation rate is higher. It must be underlined that photodegradation measured using infrared absorption corresponds to an effective degradation of the molecule. Photodegradation data obtained by UV-Vis, on the other hand, are related to a decrease in the optical absorption/emission of the probe dye. The change in the absorption/emission does not necessarily indicate a full degradation and removal of the molecule.

The experiment of photocatalysis has been reproduced three times with the same samples. The small standard deviation (Supplementary Figure S6) indicates the good reproducibility of the photocatalysis performance and the photostability of the heterostructures. Some recent works about the photodegradation properties of TiO_2 composites are summarized for comparison in Supplementary Table S1. Most of these publications focus on the photodegradation of dyes in aqueous solutions, such as methylene blue and RhB, by recording UV-Vis changes [32–38]. Actually, the full degradation of organic pollutants cannot be truly detected from the UV-Vis changes, but instead from the infrared vibrations [18,19]. On the other hand, measures performed in a liquid are far from a practical case where surfaces are required for applications. It should be underlined that a 20–35% increase in terms of photocatalytic performances in an optically transparent thin film represents a significant technological improvement.

Previous works have reported an intrinsic photocatalytic activity of WS_2 nanomaterials, which is usually measured in solutions [4,39]. However, the three WS_2 obtained in this work did not show photocatalytic degradation of stearic acid if deposited and dried on a Si wafer (see Supplementary Figure S5). Therefore, the enhancement of the photocatalytic activity measured on the TiO_2-WS_2 samples cannot be merely attributed to an additive effect of the two materials but rather to the formation of a synergistic heterostructure.

As shown in Scheme 2, the increase in the photocatalytic performances of WS_2-TiO_2 heterostructures can be explained considering the interparticle electron transfer (IPET) mechanism. According to the current knowledge, in fact, the valence band (VB) values are around −7.25 and −5.50 eV for TiO_2 and WS_2, respectively [40,41]. By coupling these values with the bandgap calculated via Tauc plots, the corresponding conduction bands (CB) can be estimated to be −3.94 and −3.65 eV for TiO_2 film and WS_2 nanosheets in our case, respectively. The band offsets allow constructing a plausible band diagram of the heterojunction. The photogenerated electrons migrate efficiently from the CB of WS_2 to that of TiO_2, while hole transfer occurs from the VB of TiO_2 to that of WS_2 [11,42]. This process results in an efficient charge separation on the hetero-interface of WS_2-TiO_2.

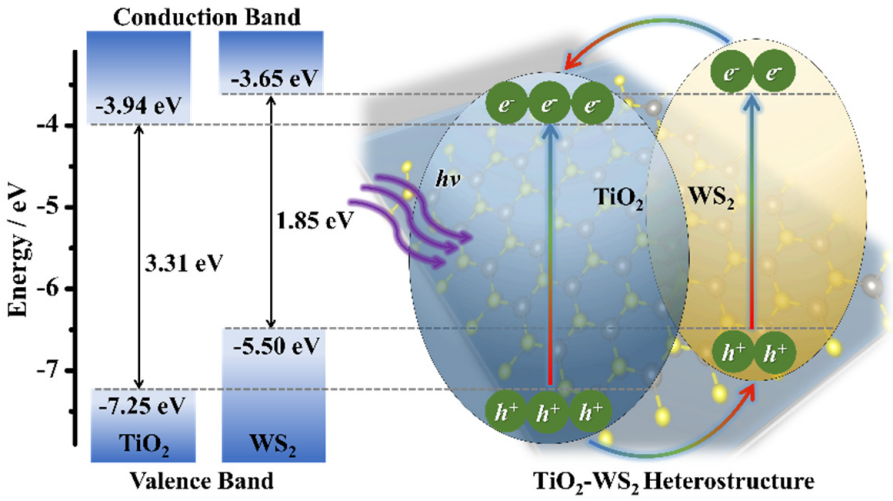

Scheme 2. Schematic illustration of the enhanced photocatalysis from the WS_2-TiO_2 heterostructure film.

3. Conclusions

Optically transparent heterostructures formed by the integration of well-dispersed WS_2 nanosheets into mesoporous ordered titania thin films have been successfully fabricated via self-assembly. The fabrication of the nanocomposite films has been achieved via two separate steps. The first one was the controlled mechanical exfoliation of WS_2 by tip-sonication to obtain few-layer nanosheets. The second stage was the addition of the WS_2 layers to the titania precursor sol to form mesoporous nanocrystalline anatase films via self-assembly. As a result, the integration of WS_2 into the titania matrix did not affect the film thickness or the organized porosity, which appeared monodispersed and well-organized throughout the matrix. In addition, controlled thermal annealing prevented WS_2 oxidation and promoted anatase formation.

The properties of WS_2-TiO_2 heterojunctions were affected by the size of the embedded 2D layers. Smaller-sized WS_2 sheets had a larger surface area that formed diffused hetero-interfaces within the porous titania structure. At the same time, the bandgap of nanosized WS_2 sheets blue-shifted towards the direct value of the WS_2 monolayer, favoring an interparticle electron transfer between the two semiconductors. Due to the fine tailoring of the WS_2-TiO_2 heterojunctions, the films showed an enhanced photocatalytic activity (+ 20% or 35%) with respect to the undoped TiO_2 and the mesoporous films containing unexfoliated WS_2. The formation of TiO_2-WS_2 heterostructures in optically transparent thin films with high photocatalytic activity represents a significant improvement for several technological applications.

4. Experimental Section

4.1. Chemicals

Crystalline tungsten (IV) sulfide powder (WS_2, 2 μm, 9%. Aldrich, St. Louis, USA), 1-Methyl-2-pyrrolidinone (NMP, 99%, Sigma-Aldrich, St. Louis, MI, USA), titanium(IV) chloride ($TiCl_4$, Aldrich, 99.9%), ethanol (EtOH, Sigma-Aldrich, 99.5%), Pluronic F-127 (∼12,600 g·mol^{-1}, Aldrich), stearic acid (Sigma-Aldrich, 97%), and deionized water were used.

4.2. Exfoliation of WS_2 Nanosheets

The WS_2 nanosheets were prepared by a sonication-assisted liquid-phase exfoliation method. The commercial WS_2 powders (WS_2-P, 250 mg) were dispersed into NMP (125 mL) and then sonicated using a probe tip for 5 h (500 W, 40% amplitude). To avoid thermal oxidation of products, the tip-pulse was on for 5 s and off for 2 s, and an ice-water bath was used to cool down the temperature of WS_2 dispersions.

The nanosheets were collected and separated in accordance with size by centrifuging at different speeds. Firstly, centrifugation at 2000 rpm for 10 min was carried out to precipitate the unexfoliated WS_2 (WS_2-U). Secondly, the supernatant was centrifugated at 4000 rpm for 10 min to precipitate the large exfoliated WS_2 (WS_2-L). Thirdly, the above supernatant was further centrifugated at 8000 rpm for 10 min to collect the small exfoliated WS_2 (WS_2-S). To remove the residual NMP, the products were washed three times by EtOH and dried at 60 °C.

4.3. Synthesis of WS_2-TiO_2 Film Heterostructures

The mesoporous films were synthesized by an evaporation-induced self-assembly method. At first, Pluronic F-127 (1.3 g) was dissolved in EtOH (46.8 mL), and $TiCl_4$ (2.2 mL) was added into the solution. After stirring for 15 min, deionized water (3.6 mL) was dropped into the mixtures. The final molar ratio was $TiCl_4$/EtOH/F-127/H_2O = 1:40:0.005:10. Then, WS_2 dispersions (500 μL, 5 mg mL^{-1} in EtOH) were added into the precursor sol (10 mL).

Silicon wafer and silica glass were used as the substrates to dip-coat films. The substrates were immersed in the WS_2 titania sols with a withdrawal rate of 10 cm min^{-1} and kept for 30 s before extraction. The relative humidity (RH) was kept under 30% by a dried airflow. Then, the obtained films were firstly dried at 60 °C in air for 10 h and then thermally annealed at 450 °C for 1 h in a nitrogen atmosphere (see Supplementary Figure S9).

4.4. Material Characterizations

Transmission electron microscopy (TEM) images were obtained by an FEI Tecnai 200 microscope working with a field emission electron gun operating at 200 kV.

Scanning electron microscope (SEM) images were captured by a ZEISS GeminiSEM 500 microscope working at an accelerating voltage of 2 kV.

Raman spectra were collected in the 65–1555 cm^{-1} range with a 3–5 cm^{-1} resolution using a Senterra confocal Raman microscope (Bruker, 633 nm laser, 0.2 mW power, and 100× objective).

The X-ray diffraction (XRD) pattern was recorded by a high-resolution diffractometer (Rigaku SmartLab X-ray diffractometer equipped with a rotating anode, 9 kW) with a Cu Kα line (λ = 1.5406 Å) operating at 40 kV and 150 mA.

Ultraviolet-visible (UV-Vis) spectra were obtained by a Nicolet Evolution 300 UV-Vis spectrophotometer (Thermo Fisher, Waltham, MA, USA) with a bandwidth of 1.5 nm.

Spectroscopic ellipsometry (α-Wollam) with fixed-angle geometry was used to measure the thickness and refractive index of the films, which were analyzed via CompleteEASE 4.2 software. A transparent model was used to calculate the refractive index.

4.5. Evaluation of Photocatalytic Activity

Stearic acid was selected as the molecular probe to evaluate the photocatalytic activity of the mesoporous WS_2-TiO_2 films. The change of vibrational modes in the 2945–2845 cm^{-1} range (-CH_2 and -CH_3 stretching) was used to characterize the photodegradation of stearic acid on different films. The process could be quantified by the corresponding integral of the infrared bands as a function of the irradiation time. Herein, Fourier transform infrared (FTIR) spectra were plotted by an infrared Vertex 70 interferometer (Bruker).

At first, stearic acid was dissolved in EtOH (3.3 mg mL^{-1}). Then, the solution (100 µL) was deposited on the films by spin-coating at 1500 rpm for 30 s. The films covered by stearic acid were irradiated under 365 nm light from a UV lamp (Spectroline, ENF-280C/FE) at a distance of 0.5 cm. The radiation time was fixed from 0 to 150 min, and FTIR spectra of these samples were recorded immediately after illumination. The photocatalysis testing has been repeated three times to prove the reproducibility of the results.

RhB was also selected as another molecular probe to verify the photocatalytic activity of WS_2-TiO_2 films by monitoring the decreasing integral intensity of absorption in the range of 450–600 nm. At first, RhB was dissolved in EtOH (10^{-5} M). Then, the RhB solution (100 µL) was deposited on the films by spin-coating at 1500 rpm for 30 s. The films covered by RhB were irradiated under 365 nm light from a UV lamp at a distance of 10 cm. The radiation time was fixed from 0 to 40 min, and absorption spectra of these samples were recorded immediately after illumination.

Supplementary Materials: The following supporting information can be downloaded at: https://www.mdpi.com/article/10.3390/nano12071074/s1, Figure S1: Raman spectra of WS_2 products; Figure S2: UV-Vis spectra of bulk WS_2; Figure S3: Thickness and refractive index of the composite films; Figure S4: UV-Vs spectra of WS_2-TiO_2 films; Figure S5: Reference spectra of photodegradation of stearic acid; Figure S6: Photodegradation of stearic acid and RhB on WS_2-TiO_2 films; Figure S7: Photodegradation of stearic acid as a function of UV exposure time; Figure S8: Photodegradation of RhB as a function of UV exposure time; Figure S9: Pictures of the experimental set-up; Table S1: Photodegradation data related to different TiO_2 photocatalysts. References [18,19,32–38] are cited in the supplementary materials.

Author Contributions: J.R.: synthesis, characterization, methodology, formal analysis, writing—original manuscript; L.S.: conceptualization, writing—review and editing, visualization, formal analysis; L.M.: methodology, formal analysis; V.P.: characterization, methodology, formal analysis; C.C.: methodology, writing—review and editing, formal analysis; S.G.: material characterization; M.M.: material characterization; P.I.: writing—original manuscript, review and editing, formal analysis, funding acquisition, project administration. All authors have read and agreed to the published version of the manuscript.

Funding: Fondazione Banco di Sardegna (Progetto MADMAT), Italian Ministry of Foreign Affairs, and International Cooperation (grant PGR07324) are gratefully acknowledged for their financial support. L.S. gratefully acknowledges the financial support received within Programma Operativo Nazionale (PON) Ricerca e Innovazione 2014–2020, Linea 1. The University of Sassari is acknowledged for funding through "Fondo di Ateneo per la Ricerca 2019".

Data Availability Statement: Original data are available upon request to the corresponding author.

Conflicts of Interest: The authors declare no competing financial interest.

References

1. Nicolosi, V.; Chhowalla, M.; Kanatzidis, M.G.; Strano, M.S.; Coleman, J.N. Liquid Exfoliation of Layered Materials. *Science* **2013**, *340*, 1226419. [CrossRef]
2. Ren, J.; Innocenzi, P. 2D Boron Nitride Heterostructures: Recent Advances and Future Challenges. *Small Struct.* **2021**, *2*, 2100068. [CrossRef]
3. Manzeli, S.; Ovchinnikov, D.; Pasquier, D.; Yazyev, O.V.; Kis, A. 2D Transition Metal Dichalcogenides. *Nat. Rev. Mater.* **2017**, *2*, 17033. [CrossRef]
4. Raza, F.; Yim, D.; Park, J.H.; Kim, H.-I.; Jeon, S.-J.; Kim, J.-H. Structuring Pd Nanoparticles on 2H-WS_2 Nanosheets Induces Excellent Photocatalytic Activity for Cross-Coupling Reactions under Visible Light. *J. Am. Chem. Soc.* **2017**, *139*, 14767. [CrossRef] [PubMed]
5. Mahler, B.; Hoepfner, V.; Liao, K.; Ozin, G.A. Colloidal Synthesis of 1T-WS_2 and 2H-WS_2 Nanosheets: Applications for Photocatalytic Hydrogen Evolution. *J. Am. Chem. Soc.* **2014**, *136*, 14121. [CrossRef]
6. Ma, Y.; Li, J.; Liu, E.; Wan, J.; Hu, X.; Fan, J. High Efficiency for H_2 Evolution and NO Removal over the Ag Nanoparticles Bridged g-C_3N_4 and WS_2 Heterojunction Photocatalysts. *Appl. Catal. B Environ.* **2017**, *219*, 467. [CrossRef]
7. Ma, X.; Chen, C.; Hu, J.; Zheng, M.; Wang, H.; Dong, S.; Huang, C.; Chen, X. Evidence of Direct Z-scheme g-C_3N_4/WS_2 Nanocomposite under Interfacial Coupling: First-Principles Study. *J. Alloy. Compd.* **2019**, *788*, 1. [CrossRef]
8. Lan, C.; Li, D.; Zhou, Z.; Yip, S.; Zhang, H.; Shu, L.; Wei, R.; Dong, R.; Ho, J.C. Direct Visualization of Grain Boundaries in 2D Monolayer WS_2 via Induced Growth of CdS Nanoparticle Chains. *Small Methods* **2019**, *3*, 1800245. [CrossRef]
9. Zhang, K.; Fujitsuka, M.; Du, Y.; Majima, T. 2D/2D Heterostructured CdS/WS_2 with Efficient Charge Separation Improving H_2 Evolution under Visible Light Irradiation. *ACS Appl. Mater. Interfaces* **2018**, *10*, 20458. [CrossRef]
10. Shi, L.; Li, Z.; Ju, L.; Carrasco-Pena, A.; Orlovskaya, N.; Zhou, H.; Yang, Y. Promoting Nitrogen Photofixation over a Periodic WS_2@TiO_2 Nanoporous Film. *J. Mater. Chem. A* **2020**, *8*, 1059. [CrossRef]
11. Cho, E.-C.; Chang-Jian, C.-W.; Zheng, J.-H.; Huang, J.-H.; Lee, K.-C.; Ho, B.-C.; Hsiao, Y.-S. Microwave-assisted Synthesis of TiO_2/WS_2 Heterojunctions with Enhanced Photocatalytic Activity. *J. Taiwan Inst. Chem. Eng.* **2018**, *91*, 489. [CrossRef]
12. Ho, W.; Yu, J.C.; Lin, J.; Yu, J.; Li, P. Preparation and Photocatalytic Behavior of MoS_2 and WS_2 Nanocluster Sensitized TiO_2. *Langmuir* **2004**, *20*, 5865. [CrossRef] [PubMed]
13. Meng, A.; Zhang, L.; Cheng, B.; Yu, J. Dual Cocatalysts in TiO_2 Photocatalysis. *Adv. Mater.* **2019**, *31*, 1807660. [CrossRef] [PubMed]
14. Jing, D.; Guo, L. WS2 Sensitized Mesoporous TiO_2 for Efficient Photocatalytic Hydrogen Production from Water under Visible Light Irradiation. *Catal. Commun.* **2007**, *8*, 795. [CrossRef]
15. Rassu, P.; Malfatti, L.; Carboni, D.; Casula, M.; Garroni, S.; Zampetti, E.; Macagnano, A.; Bearzotti, A.; Innocenzi, P. Mesoscale Organization of Titania Thin Films Enables Oxygen Sensing at Room Temperature. *J. Mater. Chem. C* **2017**, *5*, 11815. [CrossRef]
16. Classification of Titanium Dioxide Published in EU Official Journal. EUR-Lex 32020R0217. Available online: https://eur-lex.europa.eu/eli/reg_del/2020/217/oj (accessed on 24 March 2022).
17. Thomalla, M.; Tributsch, H. Photosensitization of Nanostructured TiO_2 with WS_2 Quantum Sheets. *J. Phys. Chem. B* **2006**, *110*, 12167. [CrossRef]
18. Malfatti, L.; Falcaro, P.; Pinna, A.; Lasio, B.; Casula, M.F.; Loche, D.; Falqui, A.; Marmiroli, B.; Amenitsch, H.; Sanna, R.; et al. Exfoliated Graphene into Highly Ordered Mesoporous Titania Films: Highly Performing Nanocomposites from Integrated Processing. *ACS Appl. Mater. Interfaces* **2014**, *6*, 795. [CrossRef]
19. Ren, J.; Stagi, L.; Malfatti, L.; Garroni, S.; Enzo, S.; Innocenzi, P. Boron Nitride–Titania Mesoporous Film Heterostructures. *Langmuir* **2021**, *37*, 5348. [CrossRef]
20. Liu, W.; Benson, J.; Dawson, C.; Strudwick, A.; Raju, A.P.A.; Han, Y.; Li, M.; Papakonstantinou, P. The Effects of Exfoliation, Organic Solvents and Anodic Activation on the Catalytic Hydrogen Evolution Reaction of Tungsten Disulfide. *Nanoscale* **2017**, *9*, 13515. [CrossRef]
21. Hotovy, I.; Spiess, L.; Mikolasek, M.; Kostic, I.; Sojkova, M.; Romanus, H.; Hulman, M.; Buc, D.; Rehacek, V. Layered WS_2 Thin Films Prepared by Sulfurization of Sputtered W Films. *Appl. Surf. Sci.* **2021**, *544*, 148719. [CrossRef]
22. Zeng, H.; Liu, G.-B.; Dai, J.; Yan, Y.; Zhu, B.; He, R.; Xie, L.; Xu, S.; Chen, X.; Yao, W.; et al. Optical Signature of Symmetry Variations and Spin-Valley Coupling in Atomically Thin Tungsten Dichalcogenides. *Sci. Rep.* **2013**, *3*, 1608. [CrossRef] [PubMed]
23. Wang, Q.H.; Kalantar-Zadeh, K.; Kis, A.; Coleman, J.N.; Strano, M.S. Electronics and Optoelectronics of Two-Dimensional Transition Metal Dichalcogenides. *Nat. Nanotechnol.* **2012**, *7*, 699. [CrossRef] [PubMed]

24. Sharma, S.; Bhagat, S.; Singh, J.; Singh, R.C.; Sharma, S. Excitation-Dependent Photoluminescence from WS_2 Nanostructures Synthesized via Top-Down Approach. *J. Mater. Sci.* **2017**, *52*, 11326. [CrossRef]
25. Adilbekova, B.; Lin, Y.; Yengel, E.; Faber, H.; Harrison, G.; Firdaus, Y.; El-Labban, A.; Anjum, D.H.; Tung, V.; Anthopoulos, T.D. Liquid Phase Exfoliation of MoS_2 and WS_2 in Aqueous Ammonia and their Application in Highly Efficient Organic Solar Cells. *J. Mater. Chem. C* **2020**, *8*, 5259. [CrossRef]
26. Rahmanian, E.; Malekfar, R. Size-dependent Optical Response of Few-layered WS_2 Nanosheets Produced by Liquid Phase Exfoliation. *Eur. Phys. J. Appl. Phys.* **2017**, *77*, 30401. [CrossRef]
27. Ren, J.; Malfatti, L.; Enzo, S.; Carbonaro, C.M.; Calvillo, L.; Granozzi, G.; Innocenzi, P. Boron Oxynitride Two-Colour Fluorescent Dots and their Incorporation in a Hybrid Organic-Inorganic Film. *J. Colloid Interface Sci.* **2020**, *560*, 398. [CrossRef]
28. Grosso, D.; Soler-Illia, G.J.d.A.A.; Crepaldi, E.L.; Cagnol, F.; Sinturel, C.; Bourgeois, A.; Brunet-Bruneau, A.; Amenitsch, H.; Albouy, P.A.; Sanchez, C. Highly Porous TiO_2 Anatase Optical Thin Films with Cubic Mesostructure Stabilized at 700 °C. *Chem. Mater.* **2003**, *15*, 4562. [CrossRef]
29. Arshad, Z.; Shakir, S.; Khoja, A.H.; Javed, A.H.; Anwar, M.; Rehman, A.; Javaid, R.; Qazi, U.Y.; Farrukh, S. Performance Analysis of Calcium-Doped Titania (TiO_2) as an Effective Electron Transport Layer (ETL) for Perovskite Solar Cells. *Energies* **2022**, *15*, 1408. [CrossRef]
30. Stagi, L.; Carbonaro, C.M.; Corpino, R.; Chiriu, D.; Ricci, P.C. Light Induced TiO_2 Phase Transformation: Correlation with Luminescent Surface Defects. *Phys. Status Solidi B* **2015**, *252*, 124. [CrossRef]
31. Tang, X.-Y.; Li, M.-F.; Gao, L.-F.; Yan, H.; Deng, S.-M.; Fan, J.-B.; Zheng, M.-S.; Deng, S.-L.; Zhang, Q.-Y.; Xie, S.-Y.; et al. Facile and High-Efficient Synthesis of High-Performance Supercapacitor Electrode Materials Based on the Synergistic Intercalation and Oxidation of Layered Tungsten Disulfide. *Adv. Mater. Interfaces* **2019**, *6*, 1901122. [CrossRef]
32. Zhang, Y.; Xu, J.; Mei, J.; Sarina, S.; Wu, Z.; Liao, T.; Yan, C.; Sun, Z. Strongly interfacial-coupled 2D-2D TiO_2/g-C_3N_4 Heterostructure for Enhanced Visible-light Induced Synthesis and Conversion. *J. Hazard. Mater.* **2020**, *394*, 122529. [CrossRef] [PubMed]
33. Xiao, L.; Youji, L.; Feitai, C.; Peng, X.; Ming, L. Facile Synthesis Of Mesoporous Titanium Dioxide Doped by Ag-coated Graphene with Enhanced Visible-Light Photocatalytic Performance for Methylene Blue Degradation. *RSC Adv.* **2017**, *7*, 25314. [CrossRef]
34. Li, Y.; Li, M.; Xu, P.; Tang, S.; Liu, C. Efficient Photocatalytic Degradation of Acid Orange 7 over N-doped Ordered Mesoporous Titania on Carbon Fibers under Visible-light Irradiation Based on Three Synergistic Effects. *Appl. Catal. A* **2016**, *524*, 163. [CrossRef]
35. Sheng, Y.; Yang, J.; Wang, F.; Liu, L.; Liu, H.; Yan, C.; Guo, Z. Sol-gel Synthesized Hexagonal Boron Nitride/Titania Nanocomposites with Enhanced Photocatalytic Activity. *Appl. Surf. Sci.* **2019**, *465*, 154. [CrossRef]
36. Xie, W.; Zhang, M.; Liu, D.; Lei, W.; Sun, L.; Wang, X. Reactive yellow 161 decolorization by TiO_2/porous boron nitride nanosheet composites in cotton dyeing effluent. *ACS Sustain. Chem. Eng.* **2017**, *5*, 1392. [CrossRef]
37. Bassaid, S.; Bellal, B.; Trari, M. Photocatalytic Degradation of Orange II on the novel Hetero-system WS_2/TiO_2 under UV Light. *React. Kinet. Mech. Catal.* **2015**, *115*, 389. [CrossRef]
38. Zhang, J.; Zhang, L.; Ma, X.; Ji, Z. A Study of Constructing Heterojunction between Two-dimensional Transition Metal Sulfides (MoS_2 and WS_2) and (101), (001) Faces of TiO_2. *Appl. Surf. Sci.* **2018**, *430*, 424. [CrossRef]
39. Sang, Y.; Zhao, Z.; Zhao, M.; Hao, P.; Leng, Y.; Liu, H. From UV to Near-Infrared, WS_2 Nanosheet: A Novel Photocatalyst for Full Solar Light Spectrum Photodegradation. *Adv. Mater.* **2015**, *27*, 363. [CrossRef]
40. Fujisawa, J.-i.; Eda, T.; Hanaya, M. Comparative Study of Conduction-Band and Valence-Band Edges of TiO_2, $SrTiO_3$, and $BaTiO_3$ by Ionization Potential Measurements. *Chem. Phys. Lett.* **2017**, *685*, 23. [CrossRef]
41. Cao, W.; Jiang, J.; Kang, J.; Sarkar, D.; Liu, W.; Banerjee, K. Designing Band-to-Band Tunneling Field-Effect Transistors with 2D Semiconductors for Next-Generation Low-Power VLSI. In Proceedings of the 2015 IEEE International Electron Devices Meeting (IEDM), Washington, DC, USA, 7–9 December 2015. [CrossRef]
42. Serpone, N.; Emeline, A.V. Semiconductor Photocatalysis—Past, Present, and Future Outlook. *J. Phys. Chem. Lett.* **2012**, *3*, 673. [CrossRef]